






USP8-governed GPX4 homeostasis orchestrates ferroptosis and cancer immunotherapy

Haiou Li^{a,1} , Yishuang Sun^{a,b,1}, Yingmeng Yao^{a,b,1}, Shanwen Ke^{a,b}, Nannan Zhang^c, Wenjun Xiong^{a,b}, Jie Shi^{a,b}, Chuan He^{a,b}, Xiangling Xiao^{a,b}, Haisheng Yu^{a,b} , Panpan Dai^d, Bolin Xiang^{a,b}, Xixin Xing^{a,b}, Gaoshan Xu^{a,b}, Wenjing Song^e, Jiquan Song^g, and Jinfang Zhang^{a,b,d,2} 

Edited by Eileen White, Rutgers The State University of New Jersey, New Brunswick, NJ; received September 7, 2023; accepted March 18, 2024

Ferroptosis is an iron-dependent type of regulated cell death resulting from extensive lipid peroxidation and plays a critical role in various physiological and pathological processes. However, the regulatory mechanisms for ferroptosis sensitivity remain incompletely understood. Here, we report that homozygous deletion of *Usp8* (ubiquitin-specific protease 8) in intestinal epithelial cells (IECs) leads to architectural changes in the colonic epithelium and shortens mouse lifespan accompanied by increased IEC death and signs of lipid peroxidation. However, mice with heterozygous deletion of *Usp8* in IECs display normal phenotype and become resistant to azoxymethane/dextran sodium sulfate-induced colorectal tumorigenesis. Mechanistically, USP8 interacts with and deubiquitinates glutathione peroxidase 4 (GPX4), leading to GPX4 stabilization. Thus, USP8 inhibition destabilizes GPX4 and sensitizes cancer cells to ferroptosis in vitro. Notably, USP8 inhibition in combination with ferroptosis inducers retards tumor growth and enhances CD8⁺ T cell infiltration, which potentiates tumor response to anti-PD-1 immunotherapy in vivo. These findings uncover that USP8 counteracts ferroptosis by stabilizing GPX4 and highlight targeting USP8 as a potential therapeutic strategy to boost ferroptosis for enhancing cancer immunotherapy.

USP8 | GPX4 | ubiquitination | ferroptosis | immunotherapy

Ferroptosis is a nonapoptotic form of regulated cell death that results from the accumulation of lipid peroxides in an iron-dependent manner and plays a critical role in regulating various physiological and pathological processes (1, 2). The cystine-glutamate antiporter (System xc⁻)/glutathione (GSH)/glutathione peroxidase 4 (GPX4) axis is one of the surveillance mechanisms to inhibit ferroptosis and promote tumorigenesis through converting potentially toxic phospholipid hydroperoxides to nontoxic lipid alcohols (3, 4). Increasing evidence has demonstrated that boosting ferroptosis by targeting the system xc⁻/GPX4 pathway exhibits a potential therapeutic strategy for cancer treatment (5–9). Of note, several selective small-molecule inhibitors for targeting system xc⁻ or GPX4 have been developed and displayed the potent antitumor effect through triggering ferroptosis of tumor cells in vitro and in vivo (7, 10–12). Moreover, emerging evidence suggests that these ferroptosis inducers can further strengthen the antitumor efficacy of current cancer therapies, including radiation therapy, chemotherapy, and immunotherapy, in multiple preclinical tumor models (13–16). However, the molecular regulatory mechanisms of controlling ferroptosis sensitivity and how those regulations influence tumorigenesis and cancer therapy are still largely unclear. Thus, delineating the molecular mechanisms that regulate ferroptosis holds great value in the development of previously unappreciated combination therapies for improving anticancer efficacy.

The protein ubiquitination and deubiquitination governed by ubiquitin E3 ligases and deubiquitinating enzymes (DUBs) play an important role in regulating protein homeostasis to control various biological processes (17, 18). Dysregulation of the ubiquitin system has been associated with human diseases, including cancers (19). Some DUBs are emerging as attractive therapeutic targets for cancer therapies, and increasing selective small-molecule inhibitors targeting various DUBs have been developed for cancer treatment in preclinical animal tumor models (20). Ubiquitin-specific protease 8 (USP8, also named UBPY) is a member of DUBs and frequently removes the ubiquitination from its substrates to control cellular protein fates (21). Recent studies have demonstrated that USP8 plays a critical role in regulating cell division and tumorigenesis (22–25). Additionally, investigations have revealed that USP8 confers ferroptosis resistance in liver cancer cells through different mechanisms (26, 27). However, whether USP8 regulates ferroptosis in tissue homeostasis and cancer immunotherapy remains incompletely understood.

Herein, we report that homozygous deletion of *Usp8* in intestinal epithelial cells (IECs) shortens mouse survival, accompanied by colon architectural disarray and increased lipid

Significance

Ferroptosis is pivotal in various physiological and pathological processes, yet our understanding of its mechanisms and implications for tissue homeostasis and cancer immunotherapy remains incomplete. This study elucidates the critical role of ubiquitin-specific protease 8 (USP8) in regulating lipid peroxidation and ferroptosis in colon homeostasis, tumorigenesis, and cancer immunotherapy. Specifically, we reveal that USP8 deubiquitinates glutathione peroxidase 4 (GPX4), safeguarding it from proteasome-mediated degradation. Importantly, targeting the USP8-GPX4 axis enhances the efficacy of anti-PD-1 immunotherapy in mouse tumor models, offering broad avenues for combinatorial therapeutic strategies in tumor immunotherapy.

Author contributions: H.L., Y.S., Y.Y., J. Song, and J.Z. designed research; H.L., Y.S., Y.Y., S.K., N.Z., W.X., J. Shi, C.H., X. Xiao, H.Y., P.D., B.X., X. Xing, G.X., and W.S. performed research; H.L., Y.S., Y.Y., S.K., N.Z., W.X., J. Shi, C.H., X. Xiao, H.Y., P.D., B.X., X. Xing, G.X., W.S., and J. Song analyzed data; H.L. and J.Z. wrote the paper.

The authors declare no competing interest.

This article is a PNAS Direct Submission.

Copyright © 2024 the Author(s). Published by PNAS. This article is distributed under [Creative Commons Attribution-NonCommercial-NoDerivatives License 4.0 \(CC BY-NC-ND\)](https://creativecommons.org/licenses/by-nc-nd/4.0/).

¹H.L., Y.S., and Y.Y. contributed equally to this work.

²To whom correspondence may be addressed. Email: jinfang_zhang@whu.edu.cn.

This article contains supporting information online at <https://www.pnas.org/lookup/suppl/doi:10.1073/pnas.2315541121/-DCSupplemental>.

Published April 10, 2024.

peroxidation in colon tissues. However, mice with heterozygous deletion of *Usp8* in IECs are viable and exhibit a comparable phenotype to those of wild-type (WT) mice. Heterozygous deletion of *Usp8* impedes colon tumorigenesis and tumor progression in a murine colorectal cancer model. We further find that knockdown or pharmacological inhibition of USP8 increases the sensitivity of colorectal cancer cells to ferroptosis. USP8 interacts with and deubiquitinates GPX4, thereby preventing GPX4 protein degradation. Notably, USP8 inhibition in combination with ferroptosis inducers suppresses the tumor growth and promotes CD8⁺ T cell infiltration in the tumor microenvironment, which sets up a situation that makes the PD-1/PD-L1 blockade more effective in vivo. Together, our study elucidates the physiological role of USP8 in suppressing extensive lipid peroxidation and ferroptosis via stabilizing GPX4 and highlights targeting the USP8-GPX4 axis as a potential strategy to enhance the efficacy of anti-PD-1 immunotherapy.

Results

Homozygous Deletion of *Usp8* in IECs Shortens Mouse Lifespan Accompanied by Impaired Colon Homeostasis and Increased IEC Death. Studies have shown that whole-body *Usp8* knockout in mice leads to embryonic lethality, although the underlying regulatory mechanism is still poorly understood (28). Moreover, mice with T cell-specific *Usp8* knockout spontaneously developed colitis and died within 20 wk (25). To further unravel

the physiological role of *Usp8* in mice, we generated mice with IEC-specific knockout of *Usp8* through mating mice with *loxP*-flanked (floxed, fl) *Usp8* alleles (*Usp8*^{fl/fl}) with *Villin-Cre* (*Vil-Cre*) transgenic mice (*SI Appendix, Fig. S1 A and B*). Wild-type littermates (*Usp8*^{fl/fl}), heterozygous mice (*Usp8*^{fl/+}; *Vil-Cre*), and homozygous mice (*Usp8*^{fl/fl}; *Vil-Cre*) were born with expected sex ratios and Mendelian inheritance ratios (*SI Appendix, Fig. S1 C and D*). Unexpectedly, *Usp8*^{fl/fl}; *Vil-Cre* mice exhibited dramatic growth retardation, severely reduced body weight, and shortened colon length on day 10 after birth compared with *Usp8*^{fl/fl} and *Usp8*^{fl/+}; *Vil-Cre* mice (Fig. 1 *A–C*). *Usp8*^{fl/fl}; *Vil-Cre* mice became moribund from day 5 after birth and died within 25 d, whereas there was no significant difference in survival between *Usp8*^{fl/fl} and *Usp8*^{fl/+}; *Vil-Cre* mice (Fig. 1*D* and *SI Appendix, Fig. S1D*). *Usp8*^{fl/fl} and *Usp8*^{fl/+}; *Vil-Cre* mice thrived with no remarkable abnormalities (Fig. 1 *A–D* and *SI Appendix, Fig. S1 E–I*). These results suggest that homozygous deletion of *Usp8* gene in IECs impairs colon homeostasis and causes premature death of mice.

To identify the possible cause of premature death due to *Usp8* loss, we performed the hematoxylin and eosin (H&E) staining of colon sections derived from the 10-d-old mice. Colons of *Usp8*^{fl/fl}; *Vil-Cre* mice displayed visible perturbed tissue architecture with loss of goblet cells and distortion of crypt architecture (Fig. 1*E*). In contrast, *Usp8*^{fl/+}; *Vil-Cre* mice developed a comparable mucosal appearance to that of *Usp8*^{fl/fl} mice and did not show the histopathological damage observed in colon sections of *Usp8*^{fl/fl}; *Vil-Cre* mice

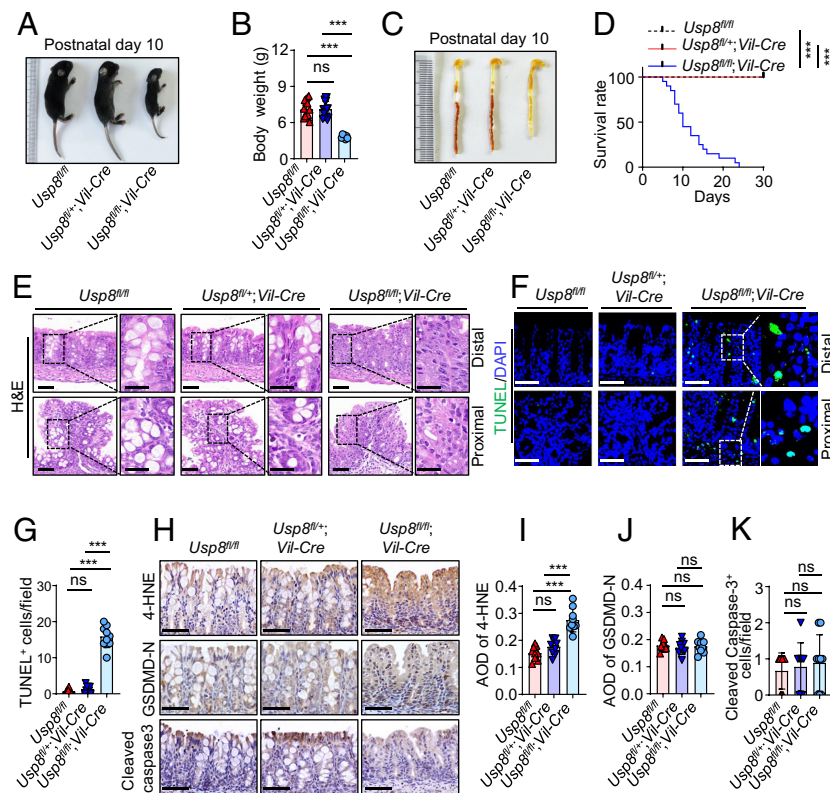


Fig. 1. Homozygous deletion of *Usp8* in IECs shortens mouse lifespan accompanied by impaired colon homeostasis and increased IEC death. (*A–D*) Representative general appearance (*A*), body weight (*B*), representative colon and rectum appearance (*C*), and survival rate (*D*) of *Usp8*^{fl/fl}, *Usp8*^{fl/+}; *Vil-Cre*, and *Usp8*^{fl/fl}; *Vil-Cre* pups. *N* = 16, 16, and 7 mice per group (*B*). *N* = 20 mice per group (*D*). (*E–G*) Representative H&E (*E*) and TUNEL (*F*) staining images of distal and proximal colon from *Usp8*^{fl/fl}, *Usp8*^{fl/+}; *Vil-Cre*, and *Usp8*^{fl/fl}; *Vil-Cre* mice at P10. The blue color indicated DAPI staining of nuclei, and the green color in nuclei indicated TUNEL-positive signals. The TUNEL-positive cells were counted in three randomly selected fields per biological replicate (*G*). *N* = 5 mice (*E*) or 3 mice (*F* and *G*) per group. (Scale bar, 50 μ m.) (*H–K*) Representative immunohistochemical (IHC) staining images of 4-HNE, cleaved-caspase 3, and N-terminal domain of GSDMD (GSDMD-N) in colons from *Usp8*^{fl/fl}, *Usp8*^{fl/+}; *Vil-Cre*, and *Usp8*^{fl/fl}; *Vil-Cre* mice at P10. [Scale bar, 50 μ m (*H*)] The 4-HNE staining (*I*) and GSDMD-N (*J*) were quantified by randomly selecting three fields per biological replicate on the basis of average optical density (AOD). The cleaved-caspase-3-positive cells (*K*) were counted in randomly selecting three fields per independent sample. *N* = 3 mice per group. In (*B*, *G*, and *I–K*), data were presented as mean \pm SD; one-way ANOVA test with Tukey's test. In (*D*), log-rank (Mantel-Cox) test was employed. ns, not significant, ****P* < 0.001.

(Fig. 1E). Remarkably, terminal deoxynucleotidyl transferase (TdT)-mediated deoxyuridine triphosphate (dUTP) Nick End Labeling (TUNEL) staining revealed an increased number of dead cells in the colon sections from *Usp8^{fl/fl};Vil-Cre* mice (Fig. 1F and G), suggesting that homozygous loss of *Usp8* might lead to IEC death. Furthermore, IHC analysis showed that the expression of 4-hydroxynonenal (4-HNE), a lipid peroxidation marker, was significantly increased in colon tissues of *Usp8^{fl/fl};Vil-Cre* mice, suggesting an increase in lipid peroxidation (Fig. 1H and I), with no significant differences in the staining of the executor of pyroptosis, N-terminal domain of GSDMD (GSDMD-N), or the apoptosis marker, cleaved caspase-3, among colon sections derived from *Usp8^{fl/fl}*, *Usp8^{fl/+}*; *Vil-Cre*, and *Usp8^{fl/fl};Vil-Cre* mice (Fig. 1H, J, and K).

Vitamin E, a lipid-soluble antioxidant, plays a pivotal role in protecting from lipid peroxidation-mediated cell death in vitro (29, 30). Importantly, previous studies have reported that vitamin E supplementation protects from detrimental lipid peroxidation in *Gpx4* null endothelial cells, hepatocytes, and IECs in mice, effectively rescuing the associated phenotypes induced by *Gpx4* depletion (31–33). To investigate whether dietary supplementation with vitamin E alleviated phenotypes induced by homozygous loss of *Usp8* (*Usp8^{fl/fl};Vil-Cre*), we employed a dietary intervention strategy. Female *Usp8^{fl/fl}* mice were mated with *Usp8^{fl/+};Vil-Cre* males, and the pregnant mice were provided with a vitamin E-enriched diet throughout gestation. The mothers were kept on this diet until the newborns were weaned, and the offspring remained on the same dietary regimen thereafter (SI Appendix, Fig. S1J). As anticipated, *Usp8^{fl/fl};Vil-Cre* mice from mothers maintained on normal diets exhibited reduced body weight and failure to thrive (SI Appendix, Fig. S1K–M). Encouragingly, *Usp8^{fl/fl};Vil-Cre* pups from mothers treated with vitamin E-enriched diets displayed improved appearance, increased body weight, and remarkably prolonged survival (SI Appendix, Fig. S1K–M). Moreover, the histomorphology of the colon in *Usp8^{fl/fl};Vil-Cre* pups from vitamin E-enriched diet treated mothers showed beneficial changes, with decreased colonic 4-HNE levels and reduced number of TUNEL-positive cells (SI Appendix, Fig. S1N–P). Collectively, these results suggest that *Usp8* plays an indispensable role in regulating IEC death, colon homeostasis, and mouse survival, which is associated with *Usp8*-restricted lipid peroxidation.

Heterozygous Deletion of *Usp8* in IECs Suppresses Tumorigenesis in Mice. To elucidate the role of *Usp8* in colorectal carcinogenesis and tumor progression, we utilized a well-established azoxymethane (AOM)/dextran sodium sulfate (DSS)-induced mouse colorectal cancer model. Both heterozygous *Usp8^{fl/+};Vil-Cre* and wild-type *Usp8^{fl/fl}* mice were treated with AOM/DSS to induce carcinogenesis (Fig. 2A). *Usp8^{fl/+};Vil-Cre* mice developed fewer and smaller tumors in the colon than *Usp8^{fl/fl}* mice, indicating that *Usp8* deficiency in IECs inhibits the colorectal tumorigenesis and tumor progression (Fig. 2B–D). Meanwhile, the *Usp8* protein levels were reduced in colon tumor tissues from *Usp8^{fl/+};Vil-Cre* mice compared to *Usp8^{fl/fl}* mice (Fig. 2E and F). Furthermore, the 4-HNE levels were significantly increased in tumor sections from heterozygous *Usp8^{fl/+};Vil-Cre* mice compared to *Usp8^{fl/fl}* mice, indicating that heterozygous deletion of *Usp8* leads to increased lipid peroxidation in tumors (Fig. 2G and H). However, GSDMD-N or cleaved caspase-3 did not show significant differences in colon sections derived from *Usp8^{fl/+};Vil-Cre* and *Usp8^{fl/fl}* mice (SI Appendix, Fig. S2A–C). To further investigate the relevance of *Usp8* depletion-mediated lipid peroxidation in tumorigenesis, we treated *Usp8^{fl/+};Vil-Cre* mice with a lipophilic radical trapping inhibitor, ferrostatin-1 (Fer-1) (Fig. 2I). Notably, Fer-1 treatment significantly accelerated tumorigenesis and tumor growth accompanied by

a decreased expression of 4-HNE in *Usp8^{fl/+};Vil-Cre* mice compared with the vehicle-treated group (Fig. 2J–O). These results reveal a crucial role of *Usp8* deletion-derived lipid peroxidation in retarding colorectal tumor progression.

Moreover, we further investigated the role of *Usp8* in lung tumor development in the *Kras^{LSL-G12D/+};Trp53^{fl/fl}* (KP) mouse model (34). To this end, the *Usp8^{fl/fl}* mice were crossed with KP mice to generate *Kras^{LSL-G12D/+};Trp53^{fl/fl};Usp8^{fl/fl}* (KPU) mice (SI Appendix, Fig. S2D and E). The lung tumorigenesis was induced by intranasal injection of adenovirus expressing Cre recombinase (Ad-Cre) (SI Appendix, Fig. S2F). We found that the tumor sizes and areas in the lungs of KPU mice were significantly smaller than those of KP mice (SI Appendix, Fig. S2G–J), indicating that *Usp8* deficiency inhibits lung tumor progression. Consistent with this, the *Usp8* protein levels were reduced in tumor tissues from KPU mice compared to KP mice (SI Appendix, Fig. S2K and L). The 4-HNE levels were significantly increased in tumor sections from KPU mice compared to KP mice (SI Appendix, Fig. S2M and N). Taken together, our results suggest that deletion of *Usp8* significantly inhibits colorectal and lung tumorigenesis and tumor progression accompanied by increased lipid peroxidation in tumors.

USP8 Inhibition Sensitizes Cancer Cells to Ferroptosis In Vitro.

Ferroptosis is a form of cell death caused by unrestricted lipid hydroperoxides. To identify potent DUBs that modulate ferroptosis sensitivity, we carried out a siRNA-based screen targeting 96 human DUBs in HCT116 cells, followed by treatment with the ferroptosis inducer erastin (Fig. 3A and B). Several previously reported DUBs that participate in ferroptosis regulation were identified, such as BAP1 (35) and OTUB1 (36) (Fig. 3B and SI Appendix, Fig. S3A), validating the robustness of this screen. Of note, we found that USP8 and USP50 were the most potent DUBs conferring resistance to erastin treatment in HCT116 cells (Fig. 3B and SI Appendix, Fig. S3A). Analyzing the correlation between gene expression and drug sensitivity using data from the Cancer Therapeutics Response Portal (CTRP) (37), we observed that the expression of *USP8*, but not *USP50*, positively and significantly correlated with resistance to multiple ferroptosis inducers, including erastin, RSL3, ML210, and ML162, in various colorectal cancer cell lines, suggesting that *USP8* may confer ferroptosis resistance in colorectal cancer cells (Fig. 3C and SI Appendix, Fig. S3B–E). In keeping with this finding, we screened a panel of DUB inhibitors, showing that the *USP8* inhibitor, DUB-IN-2, was the most potent in suppressing the cell viability and increasing cell death in HCT116 cells after treating with erastin (Fig. 3D and E). Moreover, DUB-IN-2, but not other DUB inhibitors we examined, combined with erastin treatment markedly decreased the cell viability and increased lipid peroxidation of PC9 cells (SI Appendix, Fig. S3F and G). Together, these results suggest that *USP8* inhibition may sensitize cancer cells to ferroptosis.

We further confirmed that knockdown of *USP8* decreased the viability of HCT116 and SW620 cells upon erastin and RSL3 treatments (Fig. 3F, G, J, and K and SI Appendix, Fig. S3H and I). In keeping with these results, knockdown of *USP8* in HCT116, SW620, and PC9 cells increased erastin- and RSL3-induced cell death (Fig. 3H and L and SI Appendix, Fig. S3J–M). In particular, the cell death induced by erastin or RSL3 could be almost rescued by the ferroptosis inhibitor Fer-1, but not by the apoptosis inhibitor Z-VAD-FMK (Z-V) nor necroptosis inhibitor necrostatin-1 (Nec-1) (Fig. 3H and L and SI Appendix, Fig. S3J–M). Consistent with these findings, inhibition of *USP8* by shRNAs or the pharmacologic inhibitor DUB-IN-2 significantly increased erastin- or RSL3-induced lipid peroxidation in HCT116 and SW620 cells,

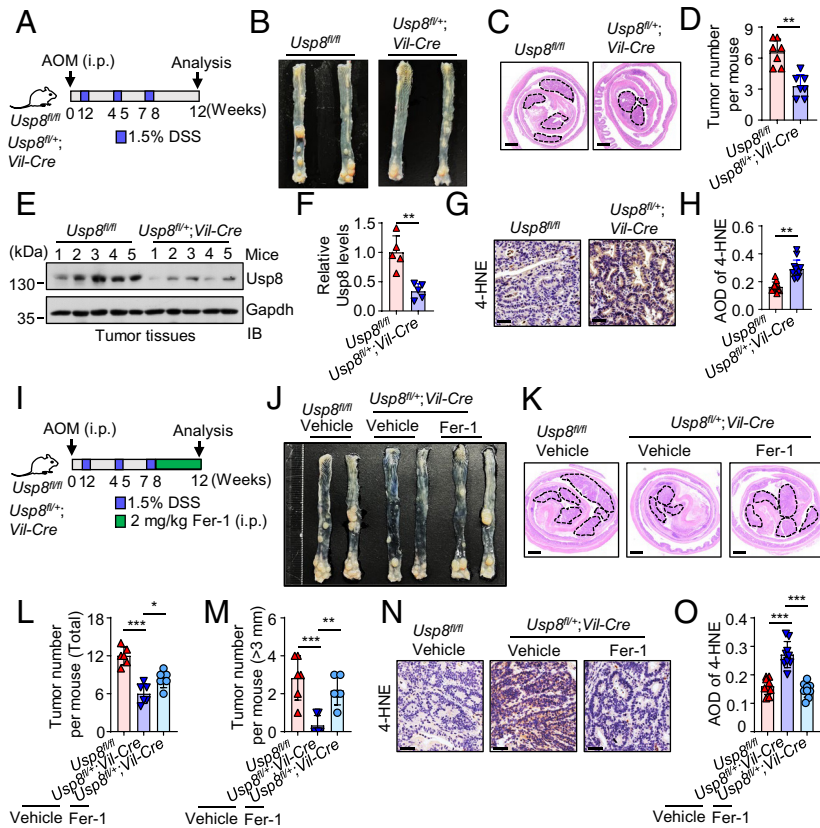


Fig. 2. Heterozygous deletion of *Usp8* in IECs suppresses colorectal tumorigenesis in mice. (A) A scheme of the AOM/DSS-induced colorectal cancer murine model. i.p., intraperitoneal. (B–D) Representative images of the tumor-burned colon and rectum (B), representative H&E staining (C), and tumor number per mouse (D) of colonic tissues from female *Usp8^{fl/fl}* and *Usp8^{fl/fl}; Vil-Cre* mice after AOM/DSS treatment. The tumor number per mouse was measured at the end of the experiment. [Scale bar, 1 mm (C).] *N* = 7 mice per group (D). (E–H) Immunoblot (IB) analysis of *Usp8* expression (E) and representative IHC staining of 4-HNE (G) in colon tumors from *Usp8^{fl/fl}* and *Usp8^{fl/fl}; Vil-Cre* mice after AOM/DSS treatment. Relative *Usp8* protein levels were quantified using ImageJ and normalized to *Gapdh* (F). [Scale bar, 50 μ m (G).] The relative 4-HNE staining was quantified by randomly selecting three fields per biological replicate on the basis of AOD (H). *N* = 4 mice per group. (I) A schematic strategy for AOM/DSS-induced colorectal tumorigenesis in *Usp8^{fl/fl}* and *Usp8^{fl/fl}; Vil-Cre* mice and subsequent ferrostatin-1 (Fer-1) treatment. The mice were intraperitoneally injected with vehicle or Fer-1 (2 mg/kg) daily with a break every 7 d. i.p., intraperitoneal. (J–O) Representative images of the tumor-burned colon and rectum (J), H&E staining of colonic tissues (K), and IHC staining of 4-HNE in tumor tissues (N) from *Usp8^{fl/fl}* and *Usp8^{fl/fl}; Vil-Cre* mice after AOM/DSS treatment. [Scale bar, 1 mm (K).] The tumor number per mouse was measured at the end of the experiment. *N* = 6 mice per group (L and M). [Scale bar, 50 μ m (N).] The relative 4-HNE staining was quantified by randomly selecting three fields per biological replicate on the basis of AOD. *N* = 3 mice per group (O). In (D, F, and H), data were presented as mean \pm SD; two-tailed unpaired *t* test. In (L, M, and O), data were presented as mean \pm SD; one-way ANOVA test with Dunnett's test. **P* < 0.05, ***P* < 0.01, ****P* < 0.001.

and the upregulation of lipid peroxidation was largely attenuated by Fer-1 (Fig. 3 *I* and *M* and *SI Appendix, Fig. S3 N–Q*). Through examining the sensitivity of several cell lines, including HCT116, SW620, PC9, and H1299, to ferroptosis inducers, our results indicated that H1299 cells were relatively more sensitive to erastin and RSL3 compared to the other three cell lines (*SI Appendix, Fig. S3 R–Y*). Furthermore, *USP8* knockdown significantly increased erastin- and RSL3-induced cell death in H1299 cells (*SI Appendix, Fig. S3 Z and ZA*). These results indicate that *USP8* inhibition increases the sensitivity of cancer cells to ferroptosis in multiple cancer cell lines.

USP8 Stabilizes GPX4 through Removing K48-Linked Ubiquitination on GPX4. To further explore the molecular mechanism of *USP8*-mediated ferroptosis regulation, we examined whether *USP8* could modulate the expression of key proteins involved in the ferroptosis pathway. Intriguingly, among the ferroptosis-related proteins we examined, *USP8* knockdown dramatically decreased the protein abundance of GPX4 in multiple cancer cell lines (Fig. 4 *A* and *B* and *SI Appendix, Fig. S4 A and B*). Additionally, our investigations in HCT116 and SW620 cells did not reveal substantial alterations in the protein expression of β -catenin and FTL upon *USP8* knockdown (Fig. 4 *A* and *B*), despite recent studies showing that *USP8* deficiency could

impact the protein levels of β -catenin and FTL in liver cancer cells (26, 27). These results suggest that the role of *USP8* in ferroptosis regulation may depend on the cellular context or cancer type. Moreover, *USP8* deficiency did not significantly affect the mRNA level of GPX4, indicating that *USP8* may function as a deubiquitinase to regulate GPX4 protein abundance at the posttranslational level (*SI Appendix, Fig. S4 C and D*). Consistently, pharmacological inhibition of *USP8* by DUB-IN-2 decreased the protein levels of GPX4 in various cancer cell lines including HCT116, SW620, PC9, and H460 (Fig. 4 *C* and *D* and *SI Appendix, Fig. S4 E and F*). To further explore the role of *USP8* in regulating GPX4, we first developed GPX4 WT and its enzymatic inactive mutant U46S (38) constructs and confirmed that overexpression of this GPX4 WT protein was functional in inhibiting RSL3-induced ferroptosis, whereas its inactive mutant GPX4 U46S had no such effect (*SI Appendix, Fig. S4 G and H*). As expected, ectopic expression of *USP8* increased the protein abundance of GPX4 (*SI Appendix, Fig. S4 I*). Furthermore, the cycloheximide (CHX)-chase assay showed that knockdown of *USP8* dramatically shortened the GPX4 protein half-life in multiple cancer cell lines, further supporting that *USP8* might regulate GPX4 protein abundance at the posttranslational level (Fig. 4 *E* and *F* and *SI Appendix, Fig. S4 J–L*).

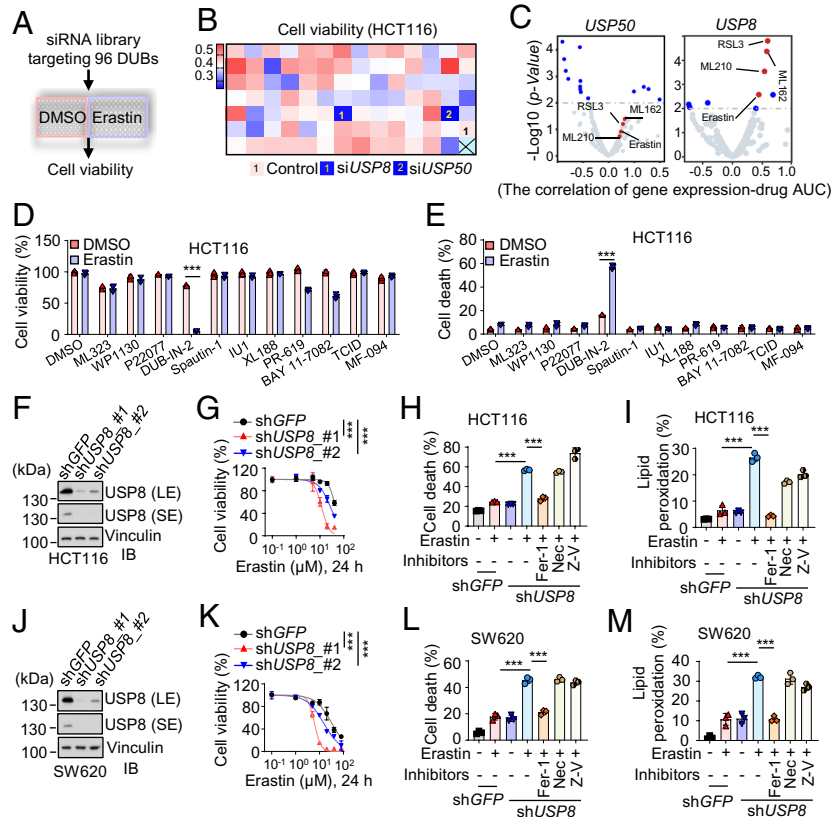


Fig. 3. USP8 inhibition sensitizes cancer cells to ferroptosis in vitro. (A) Workflow for identifying key DUBs in ferroptosis regulation. HCT116 cells were transfected with an arrayed human ON-TARGETplus siRNA library against 96 DUBs. Cell viability was measured by the CCK8 assay after 36 h treatment with DMSO or erastin (15 μ M). (B) A heatmap showing the results of RNAi-based deubiquitinating enzyme screening, pinpointing knockdown of *USP8* and *USP50* as the top-two candidates sensitize HCT116 cells to erastin treatment. Data were presented as a mean value, $N = 3$ independent biological replicates. (C) The correlation between *USP8* expression in colorectal cancer cell lines and drug sensitivities to individual compounds. Plotted data were mined from the CTRP database that contains correlation coefficients between gene expression and drug sensitivity for colorectal cancer cell lines treated with 545 compounds. Plotted values are z-scored Pearson's correlation coefficients. The drug sensitivities were determined using the AUC of the dose-response curves of the indicated compounds. (D and E) Cell viability (D) and cell death (E) were measured in HCT116 cells that were treated with erastin (10 μ M) or DMSO for 16 h, then added indicated inhibitors (2.5 μ M) or DMSO for another 9 h. (F–I) IB analysis of WCL from shGFP- or shUSP8-HCT116 cells (F). Cell viability was measured in shGFP- or shUSP8-HCT116 cells after treatment with different concentrations of erastin for 24 h (G). Cell death was assessed using PI staining in shGFP- or shUSP8-HCT116 cells exposed to erastin (20 μ M) in combination with the indicated inhibitors for 36 h (H). Lipid peroxidation was measured by BODIPYTM 581/591 C11 staining in shGFP- or shUSP8-treated HCT116 cells subjected to erastin (10 μ M) in combination with the indicated inhibitors for 24 h (I). Fer-1, 10 μ M; Necrostatin-1 (Nec), 2 μ M; Z-VAD-FMK (Z-V), 10 μ M. LE, long exposure; SE, short exposure. (J–M) IB analysis of WCL from shGFP- or shUSP8-SW620 cells (J). Cell viability was measured in shGFP- or shUSP8-SW620 cells after treatment with different concentrations of erastin for 24 h (K). Cell death was assessed in shGFP- or shUSP8-SW620 cells exposed to erastin (15 μ M) in combination with the indicated inhibitors for 36 h (L). Lipid peroxidation was measured by BODIPYTM 581/591 C11 staining in shGFP- or shUSP8-treated SW620 cells subjected to erastin (10 μ M) in combination with the indicated inhibitors for 24 h (M). Fer-1, 10 μ M; Nec, 2 μ M; Z-V, 10 μ M. In (D and E), data were presented as mean \pm SD; $N = 3$ independent biological replicates; two-tailed unpaired *t* test. In (G and K), data were presented as mean \pm SD; $N = 3$ independent biological replicates; two-way ANOVA test with Dunnett's test. In (H, I, L, and M), data were presented as mean \pm SD; $N = 3$ independent biological replicates; one-way ANOVA test with Dunnett' test. **** $P < 0.001$.

Since there are two major systems to govern protein homeostasis in cells, namely the proteasome-mediated degradation system and the autophagy-lysosome system (39), we aimed to determine the major system in regulating USP8-mediated GPX4 protein stability. Our results revealed that the proteasome inhibitor MG132, but not the lysosome inhibitors bafilomycin A1 (BafA1) nor chloroquine (CQ), almost rescued the shUSP8-mediated destabilization of GPX4 in HCT116 cells (Fig. 4G and SI Appendix, Fig. S4M). This finding suggests that USP8-mediated regulation of GPX4 homeostasis largely depends on the proteasome system. In keeping with this finding, USP8 interacted with GPX4 and removed the ubiquitination on GPX4 (Fig. 4 H–J and SI Appendix, Fig. S4 N–P). Moreover, the enzymatically inactive mutant USP8-C786A (40) failed to remove the ubiquitin chains from GPX4, suggesting that USP8 removes the ubiquitination on GPX4 through its deubiquitinating enzymatic activity (Fig. 4J). It is well known that the ubiquitin molecule can be conjugated to form distinct ubiquitin chains through one of its seven lysine (K) residues (K6, K11, K27, K29, K33, K48, and K63) (41). Our result showed that GPX4

was heavily modified by the K27- and K48-linked ubiquitination (SI Appendix, Fig. S4Q). However, ectopic expression of USP8 dramatically decreased the K48-linked ubiquitination on GPX4 while leaving the K27-linked ubiquitination unaffected, indicating that USP8 predominantly removes the K48-linked ubiquitination on GPX4 (SI Appendix, Fig. S4R). The in vivo ubiquitination assay and in vitro deubiquitination assay showed that ectopic expression of USP8 removed the K48-linked ubiquitination on GPX4 in a deubiquitinase activity-dependent manner (Fig. 4K and SI Appendix, Fig. S4S).

Previous studies have reported several lysine residues, including K48, K125, K127, K135, and K151, as potential ubiquitination sites of GPX4 (42, 43). To investigate which lysine residue of ubiquitination can be targeted by USP8, we conducted in vivo ubiquitination assays and observed that GPX4 K48R, K125R, K127R, and K151R mutants displayed a reduction in K48-linked ubiquitination (SI Appendix, Fig. S4T). Furthermore, ectopic expression of USP8 dramatically reduced the ubiquitination of GPX4 WT, K125R, K127R, and K151R mutants, but it failed

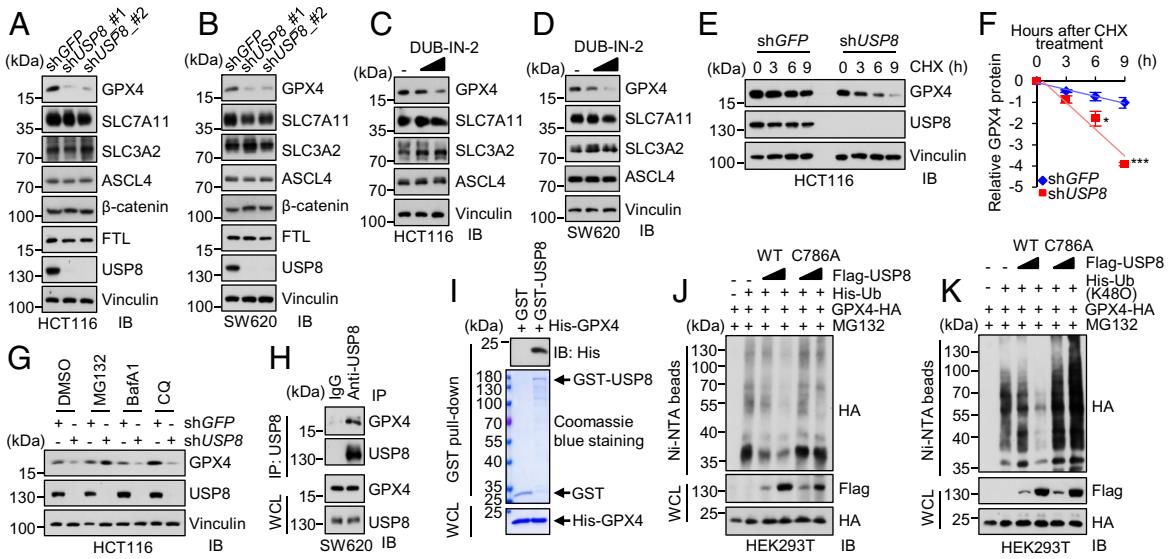


Fig. 4. USP8 stabilizes GPX4 through removing K48-linked ubiquitination on GPX4. (A and B) IB analysis of WCL from shGFP- or shUSP8-HCT116 (A) or SW620 (B) cells. (C and D) IB analysis of WCL derived from HCT116 (C) or SW620 (D) cells treated with DUB-IN-2 (1 μ M or 2 μ M) for 9 h. (E and F) IB analysis of WCL from shGFP- or shUSP8-HCT116 cells with treatment at indicated time points followed by 200 μ g/mL CHX treatment (E). GPX4 band intensity was normalized to vinculin and then compared to the $t = 0$ timepoint (F). (G) IB analysis of WCL derived from shGFP- or shUSP8-HCT116 cells treated with MG132 (10 μ M), bafilomycin A1 (BafA1, 100 nM), or chloroquine (CQ, 5 μ M) for 12 h. (H) IB analysis of WCL and anti-USP8 immunoprecipitates (IPs) derived from SW620 cells. (I) IB analysis of WCL and GST pull-down precipitates from recombinant His-GPX4 incubated with GST or GST-USP8 protein. (J and K) IB analysis of WCL and Ni-NTA pull-down products derived from lysates of HEK293T cells transfected with the indicated constructs. Cells were treated with MG132 (10 μ M) for 12 h before harvesting. Ub, ubiquitin. In (F), data were presented as mean \pm SD.; $N = 3$ independent biological replicates; two-tailed unpaired t test. * $P < 0.05$, *** $P < 0.001$.

to remove the ubiquitination of the GPX4 K48R mutant (*SI Appendix, Fig. S4U*). These results suggest that although several lysine residues on GPX4 undergo ubiquitin modification, USP8 primarily removes the ubiquitination of GPX4 at K48 residues. Taken together, these results suggest that USP8 functions as a key upstream regulator for stabilizing GPX4 largely by removing the K48-linked ubiquitination on GPX4 to prevent its proteasome-mediated degradation. However, whether other deubiquitinases target additional ubiquitination sites or ubiquitin linkage chains on GPX4 warrants further in-depth study.

USP8 Inhibition in Combination with Ferroptosis Inducers Retards Tumor Growth and Promotes CD8⁺ T Cell Infiltration.

To further explore the role of USP8 in regulating ferroptosis and cancer therapy in vivo, we evaluated the therapeutic efficacy of the USP8 inhibitor (DUB-IN-2) in combination with the ferroptosis inducer imidazole ketone erastin (IKE), an analog of erastin known for its high in vivo metabolic stability and water solubility (44–46). Our results demonstrated that DUB-IN-2 combined with IKE dramatically suppressed the subcutaneous CT26 tumor growth and increased tumoral 4-HNE levels compared to single-agent treatment (*SI Appendix, Fig. S5 A–E*). Sulfasalazine (SAS), a Food and Drug Administration-approved drug commonly used for clinical treatment, is identified as a class 1 ferroptosis inducer for in vivo treatment (14, 47). The combination of DUB-IN-2 and SAS significantly suppressed the subcutaneous CT26 tumor growth and dramatically increased 4-HNE expression in tumor tissues (Fig. 5 A–F). Moreover, the ferroptosis inhibitor, liproxstatin-1 (Lip-1) (48), significantly rescued the combination of DUB-IN-2/SAS-mediated growth retardation and reduced 4-HNE expression in inoculated CT26 tumors (*SI Appendix, Fig. S5 F–J*). Notably, through analyzing the tumor-infiltrating immune cells, we found that DUB-IN-2 in combination with SAS treatment increased the tumor-infiltrating CD8⁺ T cells, but not other immune cells we examined (Fig. 5 G and H and *SI Appendix, Fig. S5 K–M*). This result suggests that the combination therapy may reshape the tumor microenvironment to recruit CD8⁺

T cells, setting up a situation that may improve the efficiency of T cell-based immunotherapy.

To confirm these findings, we utilized the AOM/DSS-induced autochthonous colorectal tumor model to evaluate the therapeutic efficacy of SAS in *Usp8^{fl/+}; Vil-Cre* and *Usp8^{fl/fl}* mice (Fig. 5I). Remarkably, *Usp8^{fl/+}; Vil-Cre* mice exhibited the most effective tumor control when receiving SAS treatment, evidenced by a significant decrease in tumor number and size (Fig. 5 J–L and *SI Appendix, Fig. S5 N*). Moreover, the 4-HNE levels were significantly increased in tumors derived from the *Usp8^{fl/+}; Vil-Cre* mice with SAS treatment (Fig. 5 M and N). Consistent with the results in the syngeneic CT26 tumor models, the percentage of CD8⁺ T cells, but not CD4⁺ T cells, was significantly increased in tumors derived from *Usp8^{fl/+}; Vil-Cre* mice treated with SAS (Fig. 5 O and P). Additionally, *Usp8* inhibition combined with SAS treatment also significantly suppressed the primary lung cancer tumorigenesis and development in the KP mouse model (*SI Appendix, Fig. S5 O–S*). The percentage of CD8⁺ T cells was also elevated in tumor-burden lung tissues derived from KPU mice treated with SAS (*SI Appendix, Fig. S5 T and U*). These data together suggest that USP8 inhibition by its pharmacologic inhibitor or genetic deletion in combination with SAS treatment effectively suppresses tumor growth and enhances CD8⁺ T cell infiltration in tumors.

USP8 Inhibition in Combination with Ferroptosis Inducer Sensitizes Tumors to Anti-PD-1 Immunotherapy In Vivo.

Our results above demonstrated that USP8 inhibition in combination with the ferroptosis inducer SAS not only retarded the tumor growth but also increased the tumor-infiltrating CD8⁺ T cells. Thus, we speculated that USP8 inhibition in combination with SAS might enhance the efficacy of anti-PD-1 immunotherapy. To test this hypothesis, the subcutaneous CT26 murine colon tumor model was generated (Fig. 6A). Our results demonstrated that the triple combination of DUB-IN-2, SAS, and anti-PD-1 antibody significantly suppressed the CT26 tumor growth compared with the other groups (Fig. 6 B–D). Analysis of tumor-infiltrating immune cells showed that the triple therapy significantly increased

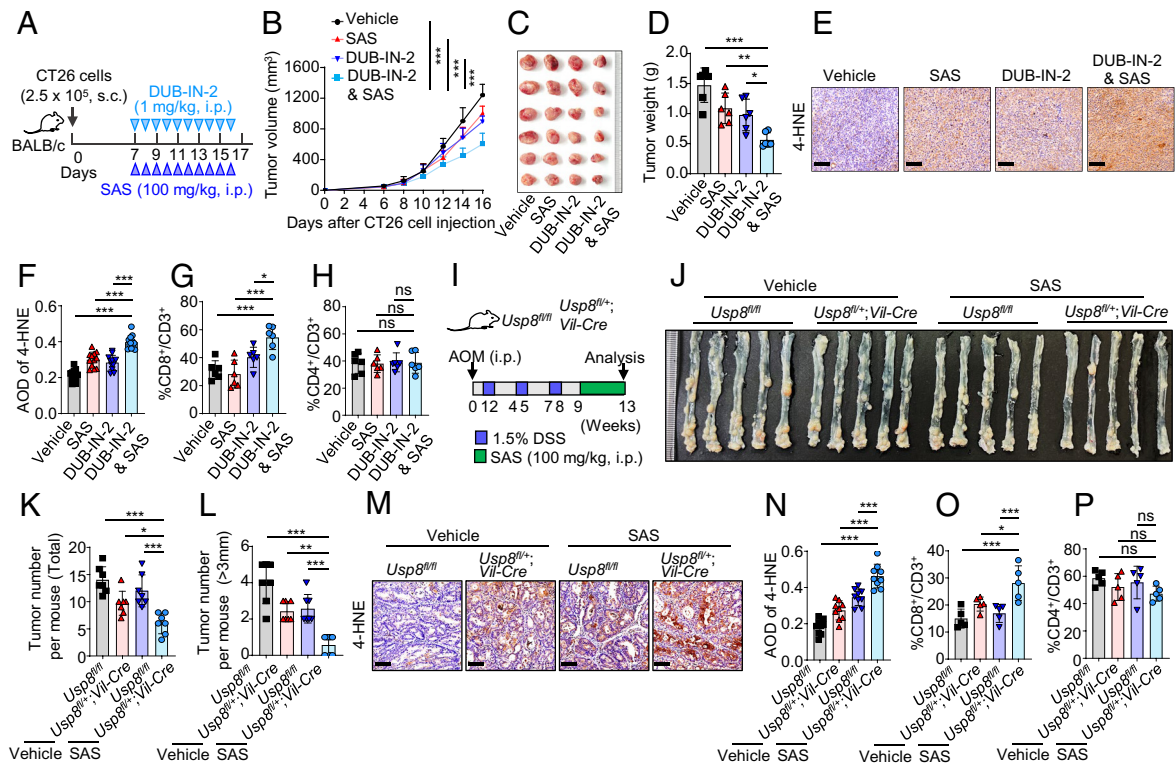


Fig. 5. USP8 inhibition in combination with ferroptosis inducer retards tumor growth and promotes tumor-infiltrating CD8⁺ T cells. (A) A schematic illustration of DUB-IN-2 and SAS treatment strategy for BALB/c mice bearing subcutaneous CT26 tumors. i.p., intraperitoneal. (B–D) The tumor growth curves (B), images of endpoint tumors (C), and endpoint tumor weight (D). *N* = 6 mice per group. (E and F) Representative images of 4-HNE IHC staining in CT26 tumor tissues from BALB/c mice with indicated treatment. [Scale bar, 100 μm (E)]. The relative optical density of 4-HNE staining was quantified by randomly selecting three fields per independent sample on the basis of AOD. (G and H) Flow cytometry analysis of the percentage of tumor-infiltrating CD8⁺ T cells (G) or CD4⁺ T cells (H) from CT26 tumors with indicated treatments. *N* = 6 mice per group. (I) A schematic strategy for AOM/DSS-induced colorectal tumorigenesis in *Usp8*^{fl/fl} and *Usp8*^{fl/+;Vil-Cre} mice and subsequent SAS treatment. The *Usp8*^{fl/fl} and *Usp8*^{fl/+;Vil-Cre} mice were intraperitoneally injected with SAS (100 mg/kg) daily with a break every 7 d. (J–M) Representative images of colon and rectum (J) and 4-HNE IHC staining in tumors (M) from *Usp8*^{fl/fl} and *Usp8*^{fl/+;Vil-Cre} mice at the end of the experiment. The tumor number per mouse was measured at the end of the experiment. *N* = 7 mice per group (K and L). [Scale bar, 100 μm (M)]. The relative 4-HNE staining was quantified by randomly selecting three fields per independent sample on the basis of AOD. *N* = 3 mice per group (N). (O and P) Flow cytometry analysis of the percentage of tumor-infiltrating CD8⁺ T cells (O) or CD4⁺ T cells (P) derived from colorectal cancer tissues of the AOM/DSS-induced mice with indicated treatment. *N* = 5 mice per group. In (B), data were presented as mean ± SD; two-way ANOVA test with Dunnett's test. In (D, F–H, K, L, and N–P), data were presented as mean ± SD; one-way ANOVA test with Dunnett's test. ns, not significant, **P* < 0.05, ***P* < 0.01, ****P* < 0.001.

the intratumoral penetration of CD8⁺ T cells, but not CD4⁺ T cells (Fig. 6 E and F). Moreover, the infiltration of IFNγ⁺ or TNF⁺ CD8⁺ T cells was also significantly increased in tumors with the triple therapy (Fig. 6 G and H).

Subsequently, we further evaluated the therapeutic efficacy of anti-PD-1 antibody in combination with SAS in inhibiting the AOM/DSS-induced colorectal tumor growth in *Usp8*^{fl/+;Vil-Cre} and *Usp8*^{fl/fl} mice (Fig. 6I). As observed in *Usp8*^{fl/fl} wild-type mice, the combined treatment of anti-PD-1 antibody and SAS moderately suppressed tumor development compared to PD-1 blockade alone (Fig. 6 J–M). However, PD-1 blockade combined with SAS treatment in *Usp8*^{fl/+;Vil-Cre} mice exerted the most potent inhibitory effect on the tumor development, significantly reducing tumor number and size in colons (Fig. 6 J–M). Consistently, anti-PD-1 therapy combined with SAS treatment displayed the most robust antitumor effects in KPU mice compared with the other groups (SI Appendix, Fig. S6 A–D). Collectively, these data suggest that the triple therapy of USP8 inhibition, SAS, and anti-PD-1 antibody remarkably retards the tumor progression in multiple murine tumor models.

Discussion

Ferroptosis plays a critical role in regulating tissue homeostasis, tumorigenesis, and cancer therapy (6, 7). Therefore, delineating the molecular mechanisms that regulate the process of ferroptosis in physiological or pathological conditions is required for designing

novel therapeutic strategies for human disease. In this study, we elucidate the role of USP8 in regulating tissue homeostasis, cancer progression, ferroptosis sensitivity, and GPX4 abundance, offering potential optimized targeting strategies for cancer treatment, such as inducing ferroptosis. Targeting the PD-1/PD-L1 axis has been widely used for treating various types of tumor (49). Increasing evidence has revealed that ferroptosis is involved in T cell immunity and cancer immunotherapy (13, 16, 29). In our study, we demonstrated that USP8 inhibition in combination with the ferroptosis inducer, SAS, significantly retarded the tumor growth and promoted the CD8⁺ T cell infiltration in the tumor microenvironment, thereby enhancing the effectiveness of anti-PD-1 immunotherapy in multiple mouse tumor models. Previous studies have demonstrated that high expression or gain of function mutations of USP8 are frequently observed in human cancers (40, 50, 51). Together with our findings, we propose a working model wherein USP8 stabilizes GPX4 through inhibiting its ubiquitination and degradation, thus decreasing the sensitivity of tumor cells to ferroptosis, promoting tumorigenesis, and conferring resistance to PD-1/PD-L1 blockade (SI Appendix, Fig. S6 E, Left). Conversely, inhibition of USP8 by genetic ablation or its pharmacological inhibitor (DUB-IN-2) down-regulates GPX4, sensitizing tumor cells to ferroptosis, retarding tumor growth, and increasing tumor-infiltrating CD8⁺ T cells that potentiates the PD-1/PD-L1 blockade therapy (SI Appendix, Fig. S6 E, Right). However, our study, along with other reports, reveals an important role of USP8 in embryonic

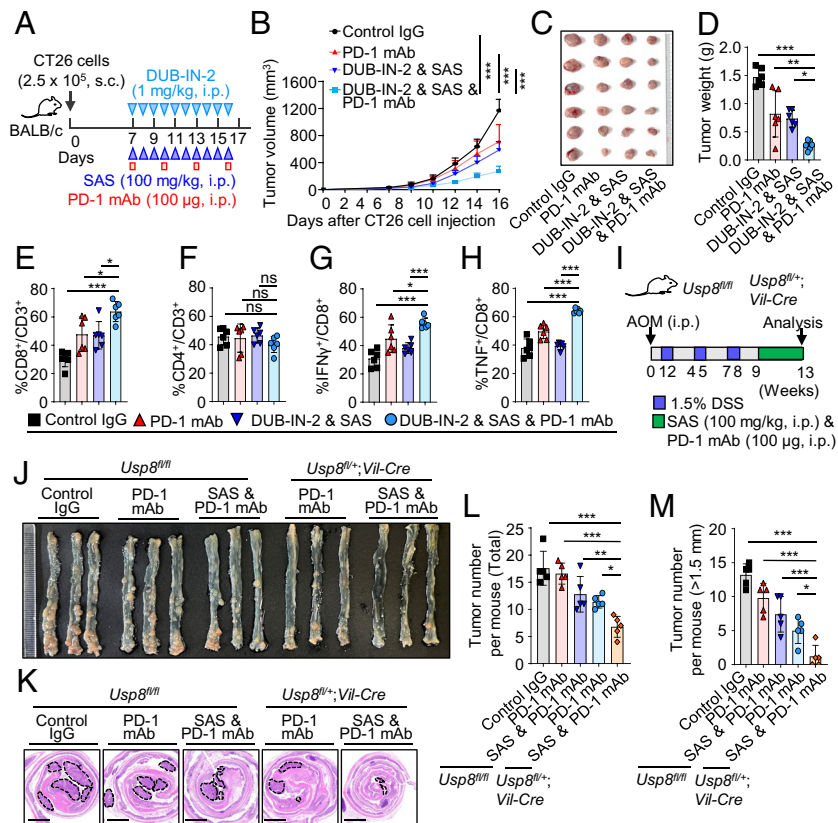


Fig. 6. USP8 inhibition in combination with ferroptosis inducer sensitizes tumors to anti-PD-1 immunotherapy in vivo. (A) A schematic illustration of the treatment strategy for BALB/c mice bearing subcutaneous CT26 tumors. Mice bearing CT26 tumors were treated with control vehicle, DUB-IN-2 (1 mg/kg) plus SAS (100 mg/kg), PD-1 mAb (100 μ g per mouse), or triple combined treatment (DUB-IN-2 plus SAS plus PD-1 mAb), respectively. i.p., intraperitoneal. mAb, monoclonal antibody. (B–D) The tumor growth curves (B), images of endpoint tumors (C), and endpoint tumor weight (D). $N = 6$ mice per group. (E–H) Flow cytometry analysis of the percentage of tumor-infiltrating CD8⁺ T cells (E), CD4⁺ T cells (F), IFN γ ⁺CD8⁺ T cells (G), or TNF⁺CD8⁺ T cells (H) from CT26 tumors with indicated treatments. $N = 6$ mice per group. (I) A schematic strategy for AOM/DSS-induced colorectal tumorigenesis in *Usp8^{fl/fl}* and *Usp8^{fl/fl};Vil-Cre* mice and treatment with SAS and PD-1 mAb. The mice were intraperitoneally injected with PD-1 mAb (100 μ g per mouse) every 3 d and SAS (100 mg/kg) daily with a break every 7 d. (J–M) Representative images of gross appearance of colon and rectum (J) and H&E staining of colorectal tumors (K) from *Usp8^{fl/fl}* and *Usp8^{fl/fl};Vil-Cre* mice at the end of the experiment. [Scale bar, 2 mm (K).] The tumor number per mouse was measured at the end of the experiment (L and M). $N = 5$ mice per group. In (B), data were presented as mean \pm SD; two-way ANOVA test with Dunnett's test. ns, not significant, * $P < 0.05$, ** $P < 0.01$, *** $P < 0.001$.

development and tissue homeostasis. Specifically, whole-body *Usp8* deletion is embryonic lethal and conditional *Usp8* deletion in IECs or T cells leads to premature death of mice. Thus, it is crucial to consider the potential side effects of systemically therapeutic targeting USP8 in the future by controlling the dosage and treatment windows.

In summary, our study not only advances our understanding of the role of USP8 in regulating ferroptosis in colon homeostasis and tumorigenesis but also highlights a potential combined therapeutic strategy for enhancing cancer treatment.

Materials and Methods

Cell Culture, Transfection, and Virus Infection. HEK293T, HCT116, SW620, PC9, A549, and H460 were cultured in Dulbecco's modified Eagle's medium (D6429, Sigma) supplemented with 10% fetal bovine serum (10437-028, Gibco) and 1% penicillin-streptomycin (SV30010, Hyclone). All cell lines were authenticated by short tandem repeats analysis and tested to ensure the absence of *Mycoplasma* contamination using MycoAlert (Lonza). Details about transfection and virus infection were described in *SI Appendix*.

Cell Viability Assay. Cells were seeded in 96-well plates with a density of 5,000 cells per well for overnight attachment and treated with different doses of erastin or RSL3 for the indicated time. The culture medium was replaced with 100 μ L fresh medium containing 10 μ L CCK8 reagent. Cells were incubated for 1 to 2 h at 37 $^{\circ}$ C, and the absorbance at 450 nm was determined using a Multiskan FC microplate reader (Thermo Fisher Scientific).

Cell Death Assay. Cells were seeded in six-well plates before treatment of the indicated drugs. After treatment, cells were collected, washed by PBS, and stained with 5 μ g/mL propidium iodide (PI) (KGA108, KeyGEN BioTECH). The dead cells that exhibited PI positivity were detected by the FACS flow cytometer (Beckman, Cytoflex) and analyzed with FlowJo 10.6.2 software.

Lipid Peroxidation Assay. Cells were seeded in 12-well plates and treated with DMSO or indicated compounds for appropriate time at 37 $^{\circ}$ C. Then, cells were harvested and suspended in PBS containing 5 μ M BODIPYTM 581/591 C11 (D3861, Invitrogen) for 30 min at 37 $^{\circ}$ C. After washing twice with PBS, cells were resuspended in cold PBS and strained through a 40 μ m cell strainer, immediately followed by flow cytometric analysis on Beckman CytoFLEX, and the signals from oxidized C11 (FITC channel) were monitored. Data were acquired on CytExpert Software 2.3. Lipid peroxidation-positive cells are defined as cells with FITC fluorescence greater than 99.9% of the unstained cancer cells.

siRNA Screening for Identifying Deubiquitinase Regulating Ferroptosis. The human ON-TARGETplus siRNA library targeting 96 human deubiquitinating enzymes (G-104705-01, Horizon Discovery) was used to perform the screen. HCT116 cells were transfected with siRNA duplexes using LipofectamineTM 3000 (L3000150, Invitrogen) according to the manufacturer's protocol. The details about siRNA transfection are provided in *SI Appendix*.

Immunoblot and Immunoprecipitation. Immunoblotting and immunoprecipitation assays were carried out as previously described (52). The information for the antibodies used for immunoblotting and immunoprecipitation is provided in *SI Appendix*.

The Protein Half-Life Analysis. To analyze GPX4 protein half-life, cells were treated with 200 $\mu\text{g}/\text{mL}$ CHX and harvested at indicated time points, followed by immunoblotting analysis of the whole-cell lysates. The signal intensity of immunoblot bands was quantified using ImageJ software. The GPX4 protein levels were normalized to vinculin. The relative amount of protein remaining at each time point was calculated by comparing it to time point 0 h.

In Vivo Ubiquitination Assay. HEK293T cells transfected with His-ubiquitin and desired constructs were treated with 10 μM MG132 for 12 h and lysed in buffer A (6 M guanidine-HCl, 0.1 M $\text{Na}_2\text{HPO}_4/\text{NaH}_2\text{PO}_4$, and 10 mM imidazole [pH 8.0]). Cell lysates were sonicated and incubated with nickel-nitrilotriacetic acid (Ni-NTA) beads (30230, QIAGEN) for 3 h at room temperature. Subsequently, Ni-NTA beads were washed twice with buffer A, twice with buffer A/TI (1 volume of buffer A and 3 volumes of TI), and once with buffer TI (25 mM Tris-HCl and 20 mM imidazole [pH 6.8]). The pull-down proteins were suspended in 30 μL 2 \times protein loading buffer, boiled for 10 min, and resolved by SDS-PAGE for immunoblotting.

GST Pull-Down Assay. Recombinant glutathione S-transferase (GST)-tagged USP8 WT and C786A were purified from *Escherichia coli* BL21. The recombinant GST-tagged proteins were purified by using glutathione-sepharose resin (17-0756-05, GE Healthcare). The details about the GST pull-down assay are provided in *SI Appendix*.

In Vivo Experimental Therapy in Mouse Tumor Models. Animal research was approved by the Institutional Animal Care and Use Committee of Wuhan University (MRI2022-LAC039, MRI2022-LAC145, MRI2022-LACA13, MRI2021-LAC28, and MRI2023-LAC167). All animal experiments were conducted according to the ethical guidelines for animals. Six-week-old female BABL/c mice were purchased from Vital River. The *Usp8* floxed (*Usp8^{fl/fl}*) mice were purchased from GemPharmaTech. *Villin-Cre* (*Vil-Cre*) transgenic mice were purchased from Cyagen Biosciences. All mice were maintained in the Specific Pathogen Free animal facility at the Medical Research Institute of Wuhan University. The details about the generation of *Usp8^{fl/fl}* mice, vitamin E supplemental feeding, subcutaneously implanted tumor models, AOM/DSS-induced colorectal cancer, the autochthonous lung tumor model, and flow cytometry analysis were incorporated in *SI Appendix*.

H&E, IHC staining, and TUNEL Staining. H&E and IHC staining were carried out as previously described (22). The information for the antibodies used for IHC staining and the details about the quantification of 4-HNE and GSDMD-N

staining are provided in *SI Appendix*. TUNEL staining was performed according to the manufacturer's protocol (11684817910, Roche), and the details are provided in *SI Appendix*.

Statistical Analysis. All data are presented as mean \pm SD of three independent experiments or biological replicates. All statistical analyses were carried out using GraphPad Prism 8.0 unless otherwise indicated. The statistical significances were analyzed using a two-tailed Student's *t* test, one-way ANOVA test, or two-way ANOVA test. The correlation between USP8 expression and the area under the curve (AUC) of the dose-response curve for indicated drugs was analyzed using Pearson's correlation coefficient. For the Kaplan-Meier survival curve, the log-rank test was used. *P* values of less than 0.05 (*P* < 0.05) were considered significant.

Data, Materials, and Software Availability. The data (Fig. 3C and *SI Appendix*, Fig. S3 B-E) were derived from the CTRP (<http://www.broadinstitute.org/ctrp/>) (53). All other data are included in the manuscript and/or *SI Appendix*.

ACKNOWLEDGMENTS. This work was supported by grants from the National Key Research and Development Program of China (2023YFC3402100 and 2022YFC3401500 to J.Z.), the National Natural Science Foundation of China (82273062 and 31970732 to J.Z. and 82103149 to H.Y.), the Major Scientific and Technological Project of Hubei Province (Grant No. 2022ACA005 to J.Z.), the Fundamental Research Funds for the Central Universities (2042022dx0003 to J.Z. and H.Y.), Knowledge Innovation Program of Wuhan-Basic Research (J.Z.), the Natural Science Foundation of Hubei Province of China (2022CFA008 to J.Z.), Translational Medicine and Interdisciplinary Research Joint Fund of Zhongnan Hospital of Wuhan University (ZJNC202312 to J.Z.), and China Postdoctoral Science Foundation (2022M722462 to H.L.). We also thank the staff at the core facility of the Medical Research Institute at Wuhan University for their technical support.

Author affiliations: ^aDepartment of Dermatology, Medical Research Institute, Frontier Science Center of Immunology and Metabolism, Zhongnan Hospital of Wuhan University, Wuhan 430071, China; ^bTaikang Center for Life and Medical Sciences, Wuhan University, Wuhan 430071, China; ^cDepartment of Radiation Oncology, The Affiliated Cancer Hospital of Zhengzhou University and Henan Cancer Hospital, Zhengzhou 450008, China; ^dDepartment of Radiation and Medical Oncology, Hubei Key Laboratory of Tumor Biological Behaviors, Hubei Cancer Clinical Study Center, Zhongnan Hospital of Wuhan University, Wuhan 430071, China; and ^eDepartment of Hepatobiliary and Pancreatic Surgery, Zhongnan Hospital of Wuhan University, Wuhan 430071, China

1. B. R. Stockwell, Ferroptosis turns 10: Emerging mechanisms, physiological functions, and therapeutic applications. *Cell* **185**, 2401-2421 (2022).
2. S. J. Dixon *et al.*, Ferroptosis: An iron-dependent form of nonapoptotic cell death. *Cell* **149**, 1060-1072 (2012).
3. G. Lei, L. Zhuang, B. Gan, Targeting ferroptosis as a vulnerability in cancer. *Nat. Rev. Cancer* **22**, 381-396 (2022).
4. W. S. Yang *et al.*, Regulation of ferroptotic cancer cell death by GPX4. *Cell* **156**, 317-331 (2014).
5. M. D. Arensman *et al.*, Cystine-glutamate antiporter xCT deficiency suppresses tumor growth while preserving antitumor immunity. *Proc. Natl. Acad. Sci. U.S.A.* **116**, 9533-9542 (2019).
6. M. A. Badgley *et al.*, Cysteine depletion induces pancreatic tumor ferroptosis in mice. *Science* **368**, 85-89 (2020).
7. M. E. Wang *et al.*, RB1-deficient prostate tumor growth and metastasis are vulnerable to ferroptosis induction via the E2F/ACSL4 axis. *J. Clin. Invest.* **133**, e166647 (2023).
8. M. J. Hangauer *et al.*, Drug-tolerant persister cancer cells are vulnerable to GPX4 inhibition. *Nature* **551**, 247-250 (2017).
9. K. Wu *et al.*, Creatine kinase B suppresses ferroptosis by phosphorylating GPX4 through a moonlighting function. *Nat. Cell Biol.* **25**, 714-725 (2023).
10. A. Ghochani *et al.*, Ferroptosis inducers are a novel therapeutic approach for advanced prostate cancer. *Cancer Res.* **81**, 1583-1594 (2021).
11. F. Yang *et al.*, Ferroptosis heterogeneity in triple-negative breast cancer reveals an innovative immunotherapy combination strategy. *Cell Metab.* **35**, 84-100.e8 (2023).
12. C. Conche *et al.*, Combining ferroptosis induction with MDSC blockade renders primary tumours and metastases in liver sensitive to immune checkpoint blockade. *Gut* **72**, 1774-1782 (2023), 10.1136/gutjnl-2022-327909.
13. P. Liao *et al.*, CD8(+) T cells and fatty acids orchestrate tumor ferroptosis and immunity via ACSL4. *Cancer Cell* **40**, 365-378.e6 (2022).
14. G. Lei *et al.*, The role of ferroptosis in ionizing radiation-induced cell death and tumor suppression. *Cell Res.* **30**, 146-162 (2020).
15. X. Lang *et al.*, Radiotherapy and immunotherapy promote tumoral lipid oxidation and ferroptosis via synergistic repression of SLC7A11. *Cancer Discov.* **9**, 1673-1685 (2019).
16. W. Wang *et al.*, CD8(+) T cells regulate tumour ferroptosis during cancer immunotherapy. *Nature* **569**, 270-274 (2019).
17. B. Dale *et al.*, Advancing targeted protein degradation for cancer therapy. *Nat. Rev. Cancer* **21**, 638-654 (2021).
18. F. Dang, L. Nie, W. Wei, Ubiquitin signaling in cell cycle control and tumorigenesis. *Cell Death Differ.* **28**, 427-438 (2021).
19. D. Popovic, D. Vucic, I. Dikic, Ubiquitination in disease pathogenesis and treatment. *Nat. Med.* **20**, 1242-1253 (2014).
20. J. A. Harrigan, X. Jacq, N. M. Martin, S. P. Jackson, Deubiquitylating enzymes and drug discovery: Emerging opportunities. *Nat. Rev. Drug Discov.* **17**, 57-78 (2018).
21. S. M. Lange, L. A. Armstrong, Y. Kulathu, Deubiquitinases: From mechanisms to their inhibition by small molecules. *Mol. Cell* **82**, 15-29 (2022).
22. W. Xiong *et al.*, USP8 inhibition reshapes an inflamed tumor microenvironment that potentiates the immunotherapy. *Nat. Commun.* **13**, 1700 (2022).
23. H. Peng *et al.*, The ubiquitin-specific protease USP8 directly deubiquitinates SQSTM1/p62 to suppress its autophagic activity. *Autophagy* **16**, 698-708 (2020).
24. J. Mathieu, P. Michel-Hissier, V. Boucherit, J. R. Huynh, The deubiquitinase USP8 targets ESCRT-III to promote incomplete cell division. *Science* **376**, 818-823 (2022).
25. A. Dufner *et al.*, The ubiquitin-specific protease USP8 is critical for the development and homeostasis of T cells. *Nat. Immunol.* **16**, 950-960 (2015).
26. J. N. Tang, G. Long, L. Xiao, L. D. Zhou, USP8 positively regulates hepatocellular carcinoma tumorigenesis and confers ferroptosis resistance through β -catenin stabilization. *Cell Death Dis.* **14**, 360 (2023).
27. L. H. Liu *et al.*, Suppression of USP8 sensitizes cells to ferroptosis via SQSTM1/p62-mediated ferritinophagy. *Protein Cell* **14**, 230-234 (2023).
28. S. Miendorf *et al.*, Essential role of ubiquitin-specific protease 8 for receptor tyrosine kinase stability and endocytic trafficking in vivo. *Mol. Cell Biol.* **27**, 5029-5039 (2007).
29. X. Jiang, B. R. Stockwell, M. Conrad, Ferroptosis: Mechanisms, biology and role in disease. *Nat. Rev. Mol. Cell Biol.* **22**, 266-282 (2021).
30. A. Seiler *et al.*, Glutathione peroxidase 4 senses and translates oxidative stress into 12/15-lipoxygenase dependent- and AIF-Mediated cell death. *Cell Metab.* **8**, 237-248 (2008).
31. M. Wortmann *et al.*, Combined deficiency in glutathione peroxidase 4 and vitamin E causes multiorgan thrombus formation and early death in mice. *Circ. Res.* **113**, 408-417 (2013).
32. B. A. Carlson *et al.*, Glutathione peroxidase 4 and vitamin E cooperatively prevent hepatocellular degeneration. *Redox Biol.* **9**, 22-31 (2016).
33. L. Mayr *et al.*, Dietary lipids fuel GPX4-restricted enteritis resembling Crohn's disease. *Nat. Commun.* **11**, 1775 (2020).

34. M. Zhang *et al.*, CCL7 recruits cDC1 to promote antitumor immunity and facilitate checkpoint immunotherapy to non-small cell lung cancer. *Nat. Commun.* **11**, 6119 (2020).
35. Y. Zhang *et al.*, BAP1 links metabolic regulation of ferroptosis to tumour suppression. *Nat. Cell Biol.* **20**, 1181–1192 (2018).
36. T. Liu, L. Jiang, O. Tavana, W. Gu, The deubiquitylase OTUB1 mediates ferroptosis via stabilization of SLC7A11. *Cancer Res.* **79**, 1913–1924 (2019).
37. M. G. Rees *et al.*, Correlating chemical sensitivity and basal gene expression reveals mechanism of action. *Nat. Chem. Biol.* **12**, 109–116 (2016).
38. I. Ingold *et al.*, Selenium utilization by GPX4 is required to prevent hydroperoxide-induced ferroptosis. *Cell* **172**, 409–422.e21 (2018).
39. A. Varshavsky, The ubiquitin system, autophagy, and regulated protein degradation. *Annu. Rev. Biochem.* **86**, 123–128 (2017).
40. S. Shin *et al.*, Deubiquitylation and stabilization of Notch1 intracellular domain by ubiquitin-specific protease 8 enhance tumorigenesis in breast cancer. *Cell Death Differ.* **27**, 1341–1354 (2020).
41. S. Kolla, M. Ye, K. G. Mark, M. Rape, Assembly and function of branched ubiquitin chains. *Trends Biochem. Sci.* **47**, 759–771 (2022).
42. J. B. Li *et al.*, Tumor-specific GPX4 degradation enhances ferroptosis-initiated antitumor immune response in mouse models of pancreatic cancer. *Sci. Transl. Med.* **15**, eadg3049 (2023).
43. H. R. Liu *et al.*, Characterization of a patient-derived variant of GPX4 for precision therapy. *Nat. Chem. Biol.* **18**, 91–100 (2022).
44. M. H. Larraufie *et al.*, Incorporation of metabolically stable ketones into a small molecule probe to increase potency and water solubility. *Bioorg. Med. Chem. Lett.* **25**, 4787–4792 (2015).
45. Y. Zhang *et al.*, Imidazole ketone erastin induces ferroptosis and slows tumor growth in a mouse lymphoma model. *Cell Chem. Biol.* **26**, 623–633.e9 (2019).
46. D. Liang *et al.*, Ferroptosis surveillance independent of GPX4 and differentially regulated by sex hormones. *Cell* **186**, 2748–2764.e22 (2023).
47. P. W. Gout, A. R. Buckley, C. R. Simms, N. Bruchovsky, Sulfasalazine, a potent suppressor of lymphoma growth by inhibition of the x(c)- cystine transporter: A new action for an old drug. *Leukemia* **15**, 1633–1640 (2001).
48. J. P. Friedmann Angeli *et al.*, Inactivation of the ferroptosis regulator Gpx4 triggers acute renal failure in mice. *Nat. Cell Biol.* **16**, 1180–1191 (2014).
49. X. He, C. Q. Xu, Immune checkpoint signaling and cancer immunotherapy. *Cell Res.* **30**, 660–669 (2020).
50. S. Byun *et al.*, USP8 is a novel target for overcoming gefitinib resistance in lung cancer. *Clin. Cancer Res.* **19**, 3894–3904 (2013).
51. Z. Y. Ma *et al.*, Recurrent gain-of-function USP8 mutations in Cushing's disease. *Cell Res.* **25**, 306–317 (2015).
52. C. He *et al.*, UFL1 ablation in T cells suppresses PD-1 UFMylation to enhance anti-tumor immunity. *Mol. Cell* **84**, 1120–1138.e8 (2024), 10.1016/j.molcel.2024.01.024.
53. B. Seashore-Ludlow *et al.*, Cancer Therapeutics Response Portal (CTRP v2, 2015) dataset: 545 small molecules and select combinations; 907 cancer cell lines (CCLs). CTRP. <http://www.broadinstitute.org/ctrp/>. Accessed 10 July 2023.